npj Precision Oncology

https://doi.org/10.1038/s41698-026-01382-5

Article in Press

AI-driven body composition atlas reveals its association with NSCLC immunotherapy outcome and molecular background: a multicenter study

Received: 3 December 2025

Accepted: 12 March 2026

Cite this article as: Guo, Y., Gong, B., Lou, J. *et al.* AI-driven body composition atlas reveals its association with NSCLC immunotherapy outcome and molecular background: a multicenter study. *npj Precis. Onc.* (2026). https://doi.org/10.1038/s41698-026-01382-5

Yusheng Guo, Bingxin Gong, Jie Lou, Li Wan, Ying-Long Peng, Yiqun Chen, Xiaoyan Lei, Peng Mo, Qi Wan, Qing Sun, Shu Peng, Chuansheng Zheng & Lian Yang

AI-Driven Body Composition Atlas Reveals Its Association with NSCLC Immunotherapy Outcome and Molecular Background: A Multicenter Study

Yusheng Guo[1,2,3#], Bingxin Gong[1,2,3#], Jie Lou[1,2,3#], Li Wan[4], Ying-Long Peng[5], Yiqun Chen[6], Xiaoyan Lei[7], Peng Mo[8], Qi Wan[9], Qing Sun[1,2,3], Shu Peng[10*], Chuansheng Zheng[1,2,3*], Lian Yang[1,2,3*]

[1]Department of Radiology, Union Hospital, Tongji Medical College, Huazhong University of Science and Technology, Wuhan, 430022, China.

[2]Hubei Provincial Clinical Research Center for Precision Radiology & Interventional Medicine，Wuhan, 430022, China.

[3]Hubei Key Laboratory of Molecular Imaging, Wuhan, 430022, China.

[4]Department of Thoracic Surgery, Union Hospital, Tongji Medical College, Huazhong University of Science and Technology, Wuhan 430022, China.

[5]Guangdong Lung Cancer Institute, Guangdong Provincial People's Hospital (Guangdong Academy of Medical Sciences), Southern Medical University, Guangzhou 510055, China

[6]Department of Respiratory and Critical Care Medicine, Affiliated Hospital of Nantong University, Medical School of Nantong University, Nantong 226001, China.

[7]Department of Radiology, Hainan General Hospital, Hainan Affiliated Hospital of Hainan Medical University, Haikou 570102, China.

[8]Department of Radiotherapy, 900th hospital of Joint Logistics Support Force; Fuzhou, China, 350025.

[9]Department of Radiology, the Key Laboratory of Advanced Interdisciplinary Studies Center, National Center for

Respiratory Medicine, the First Affiliated Hospital of Guangzhou Medical University, Guangzhou 510120, China.

[10]Department of Thoracic Surgery, Tongji Hospital, Tongji Medical College, Huazhong University of Science and Technology, Wuhan 430030, China.

[#] Yusheng Guo, Bingxin Gong and Jie Lou contributed equally.

[*]**Correspondence:**

Lian Yang, Department of Radiology, Union Hospital, Tongji Medical College, Huazhong University of Science and Technology, No.1277 Jiefang Avenue, Wuhan 430022, China; E-mail: yanglian@hust.edu.cn;

Chuansheng Zheng, Department of Radiology, Union Hospital, Tongji Medical College, Huazhong University of Science and Technology, No.1277 Jiefang Avenue, Wuhan 430022, China; E-mail: hqzcsxh@sina.com;

Shu Peng, Department of Thoracic Surgery, Tongji Hospital, Tongji Medical College, Huazhong University of Science and Technology, No.1095 Jiefang Avenue, Wuhan 430030, China; Email: drpeng90@hotmail.com.

Abstract

Although previous studies have linked body composition to immunotherapy efficacy, comprehensive multidimensional analyses with biological explanations remain lacking. This study integrated eight independent cohorts comprising 2,132 non-small cell lung cancer (NSCLC) patients, including five immune checkpoint inhibitor prognostic cohorts (n=1,919), two bulk RNA-seq cohorts (n=190), and one prospective single-cell RNA-seq cohort (n=23). Using deep learning algorithms, we automatically extracted 92 body composition parameters from computed tomography images. The AI-based segmentation system demonstrated high consistency with manual measurements (intraclass correlation coefficient >0.87) with significantly improved efficiency. In male patients, higher intermuscular fat volume (IMFV) and 14 other indicators were independent predictors of overall survival; in female patients, T12 subcutaneous fat density and 6 other indicators showed potential associations with survival. Male patients with high IMFV exhibited significant upregulation of interferon-related pathways in CD8+ T cells and NK cells, along with lower exhaustion scores, while female patients with high T12 subcutaneous fat density showed macrophage polarization toward the M1 phenotype. This study underscores the importance of multidimensional body composition in NSCLC patient management, demonstrating that specific parameters are not only closely related to survival outcomes but also exhibit unique gender differences and location variations, providing new insights for optimizing immunotherapy strategies.

Keywords: Non-small Cell Lung Cancer; Transcriptomics; Body Composition; Artificial Intelligence; Immunotherapy

Introduction

Non-small cell lung cancer (NSCLC), one of the most prevalent and lethal malignancies worldwide [1], represents a major public health challenge. In recent years, the emergence of immune checkpoint inhibitors (ICIs) has profoundly reshaped the treatment paradigm for NSCLC [2]. However, not all patients benefit from this therapy, as its efficacy is

influenced by multiple factors [3], including the tumor microenvironment, gene expression profiles, and systemic host conditions [4,5]. Among these factors, body composition has increasingly drawn research interest [6]. Beyond reflecting nutritional status and musculoskeletal health, body composition may also be intricately linked to tumor biology and treatment response [7,8]. Although prior studies have shown that traditional indicators like body mass index (BMI) are associated with cancer prognosis, particularly in immunotherapy, where the complex relationship between BMI and treatment outcomes is termed the "obesity paradox" [9,10]. These metrics are often oversimplified and fail to comprehensively capture the multidimensional nature of body composition. Therefore, developing a more refined and comprehensive method for measuring body composition and exploring its relationship with clinical outcomes in NSCLC patients receiving ICIs holds significant clinical value.

Previous research has primarily relied on single body composition metrics, such as BMI or muscle mass [11-13], offering limited insights into the complex interplay between tumors and body composition. In fact, body composition is a multifaceted concept encompassing various tissue types, including but not limited to subcutaneous fat, visceral fat, skeletal muscle, and intermuscular fat [14]. Each component may influence cancer development and progression through distinct biological mechanisms. For example, sarcopenia has been associated with poorer survival outcomes across multiple cancers [15], while adipose tissue serves not only as an energy reservoir but also as an active endocrine organ [16], secreting bioactive substances that regulate modulate inflammation and immune responses [17]. Given this complexity, there is an urgent need for advanced analytical methods to accurately quantify and evaluate these diverse components. Furthermore, advancements in high-throughput sequencing technologies now enable the concurrent analysis of tumor genetic profiles and detailed body composition features, thereby uncovering potential interactions between them. These developments present unprecedented opportunities to investigate how body composition influences immunotherapy efficacy in NSCLC patients.

To systematically address this gap, we designed a comprehensive, multimodal study integrating CT imaging, bulk RNA sequencing (RNA-seq), and single-cell RNA sequencing (scRNA-seq) to investigate the impact of multidimensional body composition on immunotherapy outcomes in NSCLC patients. First, we developed a deep learning-based segmentation system to automatically extract 92 two- and three-dimensional body composition parameters from CT images, including vertebrae, subcutaneous fat, skeletal muscle, intermuscular fat, and visceral fat. This approach enhances measurement precision while substantially increasing processing efficiency and minimizing human error. Subsequently, we analyzed data from eight independent cohorts (2,132 patients) including: (1) five multi-center ICI prognostic cohorts (n=1,919) were used to evaluate associations between body composition features and survival outcomes; (2) two bulk RNA-seq cohorts, the NSCLC-Radiogenomics cohort and TCGA-LUAD/LUSC patients with available CT imaging (n=190), served as bridges to link imaging-derived body composition metrics with tumor immune phenotypes; (3) one prospective scRNA-seq cohort (n=23) was employed for hypothesis-generating exploration of cellular-level immune states associated with specific body composition profiles. Our study systematically explored the associations between body composition and patient survival, and further uncovered distinct immune landscape alterations associated with specific body composition profiles, providing new insights into their role in shaping anti-tumor immunity **(Figure 1)**.

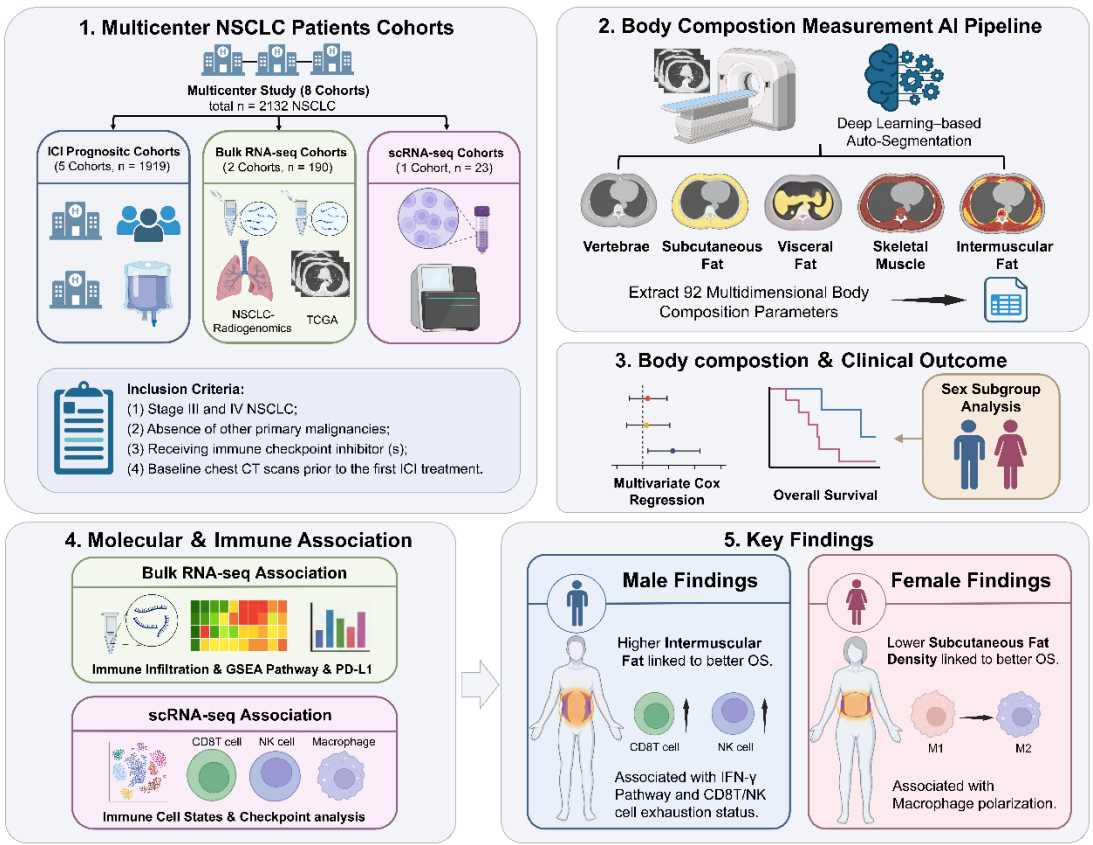

Figure 1. Workflow and key findings of this study.

Results

Study design and patients

This study included 2,132 NSCLC patients from eight independent cohorts. Among them, 1,919 patients with available CT imaging, clinical data, and prognostic information from five cohorts were used to evaluate the association between multidimensional body composition and clinical outcomes following immunotherapy **(Table S1)**. Two cohorts comprising 190 patients with paired CT images and bulk RNA-seq data were utilized to explore relationships between body composition and tumor microenvironment characteristics. An additional cohort of 23 patients with matched CT imaging and scRNA-seq data enabled in-depth investigation of body composition-tumor molecular background

correlations. The study population consisted of 84.8% males (n=1629) and 15.2% females (n=290) for the ICI-treated clinical cohorts. The median age was 64 years (IQR 58-69) for the overall cohort, with sex-specific distributions of 65 years (IQR 59-70) for male patients and 59 years (IQR 51-66) for female patients.

Correlations of body composition parameters in NSCLC patients

Previous studies have reported sex differences in body composition [18]. Consistent with this, our 3D analysis revealed that male patients had significantly higher SMV and vertebral body volume (VBV) **(Figure S1)**, while female patients had significantly higher SFV. No sex difference was observed in IMFV **(Figure 2A)**. We further identified that SMV was negatively correlated with age, whereas IMFV showed a positive correlation with age; SFV demonstrated no significant association with age **(Figure 2B)**. Additionally, SFV, SMV, and IMFV all increased with higher BMI **(Figure S2A-C)**. Based on 2D body composition measurements from individual vertebral levels **(Figure 2C)**, we conducted a comprehensive correlation analysis. For parameters measured at the same level, similar types of parameters, such as SMA, skeletal muscle density (SMD), and skeletal muscle index (SMI), showed strong correlations; similar for fat-related parameters **(Figure 2D, Figure S3-S4)**. Within the same category of parameters, even across different vertebral levels, there was a very strong correlation, a pattern observed consistently across all measured parameters **(Figure 2D, Figure S5-S6)**.

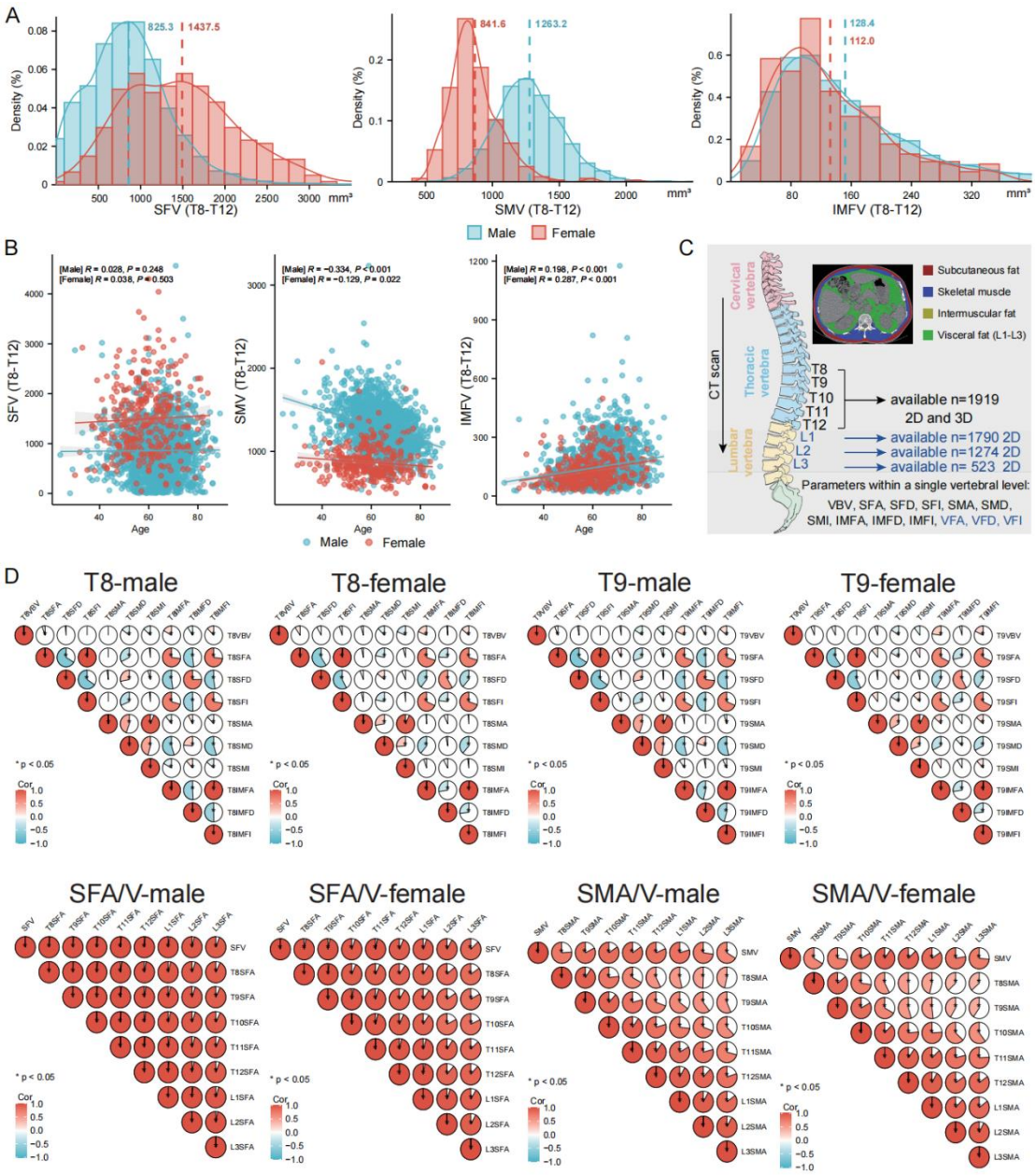

Figure 2. Correlations of body composition parameters in NSCLC patients. (A) Distribution patterns of subcutaneous fat volume (SFV), skeletal muscle volume (SMV), and intermuscular fat volume (IMFV) stratified by gender. (B) Correlation analyses between SFV/SMV/IMFV and age. (C) CT scanning ranges and corresponding sample sizes. (D) Correlation analysis of different body composition parameters at the same anatomical level (upper panel), and correlation analysis of the same body composition parameter across different levels (lower panel).

Association between multidimensional thoracic body composition and survival outcomes

Consistent with previous reports linking BMI to immunotherapy outcomes [19], we observed that patients with a BMI > 20.9 had longer OS after immunotherapy **(Figure S7A)**, but this association was not significant when BMI was analyzed using the median cutoff **(Figure S7B)**. To systematically evaluate the association between diverse body composition parameters and OS, we generated a heatmap based on their performance as continuous variables in univariate Cox regression analysis. During follow-up, 712 deaths (43.7%) occurred in the male subgroup and 135 (46.5%) in the female subgroup. In male patients, increased IMFV, IMFA, intermuscular fat index (IMFI), VBV, and T11 subcutaneous fat area (T11SFA) were associated with improved OS, while decreased subcutaneous fat density (SFD), T11SMD, T12SMD, and T9SMI were also linked to longer survival **(Figure 3A)**. When the cutoff value for IMFV was set at 0.196, the difference between survival curves was maximized. We also found that the risk of death decreased with increasing IMFV after adjusting for age and BMI. Similarly, the largest survival difference was observed when T8VBV was set at 32.3, and the risk of death decreased as T8VBV increased **(Figure 3B)**. Notably, when IMFV and T8VBV were dichotomized using median-based stratification, the survival curves remained significantly different **(Figure S8A)**. RCS plots further illustrated the relationships for T12SFD and T11IMFA **(Figure S9A)**. In female patients, lower levels of T12SFD, T9 intermuscular fat density (T9IMFD), T10IMFD, and T12IMFD were associated with improved OS **(Figure 3C)**. Survival differences were most pronounced at a T12SFD cutoff of -90.8, though its positive association with mortality risk was not statistically significant after adjusting for age and BMI. Similarly, the largest survival difference occurred when T9IMFD was set at -70.3, with increasing mortality risk as T9IMFD increased **(Figure 3D)**. Similar results were observed when patients were stratified using the median value **(Figure S8B)**. We also analyzed the optimal cutoff values for T10IMFD and T12IMFD and presented RCS plots **(Figure S9B)**.

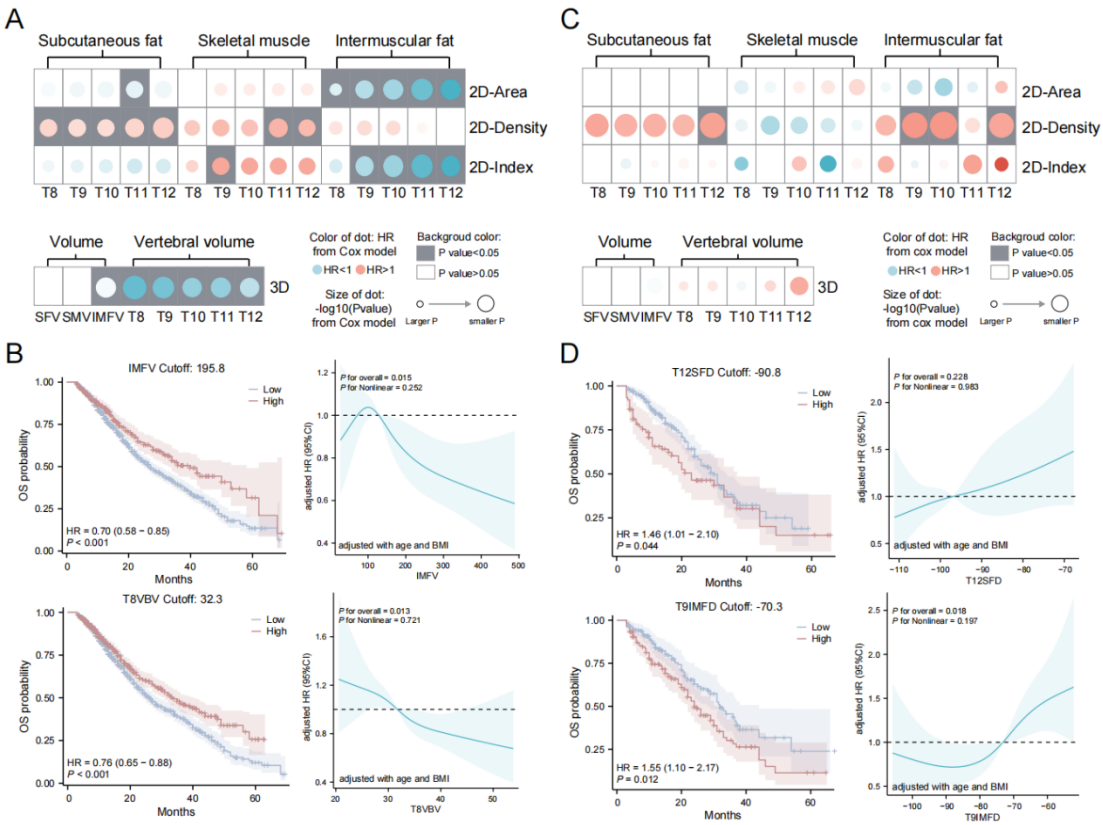

Figure 3. Association between multidimensional thoracic body composition and survival outcomes. (A) The heatmap shows the results of univariate Cox regression analysis between multidimensional thoracic body composition parameters and clinical outcomes in males. (B) Survival curves illustrate survival differences based on specific thoracic body composition parameters in male patients, and restricted cubic spline plots depict the overall association between specific thoracic body composition parameters and survival in male patients. (C) The heatmap shows the results of univariate Cox regression analysis between multidimensional thoracic body composition parameters and clinical outcomes in females. (D) Survival curves illustrate survival differences based on specific thoracic body composition parameters in female patients, and restricted cubic spline plots depict the overall association between specific thoracic body composition parameters and survival in female patients.

Association Between Multidimensional Abdominal Body Composition and Survival Outcomes

Given that the L3 level is widely regarded as a representative cross-sectional level for body composition, we extended our analysis to include body composition parameters at the L1 – L3 vertebral levels, thereby incorporating

measurements of visceral adipose tissue. We found that in male patients, an increase in L1SFA was associated with a decrease in mortality, while increases in SFD at L1, L2, and L3, VFD at L1 and L2, and L3 IMFD were linked to higher mortality **(Figure 4A)**. Similarly, we explored the optimal cutoff values for these indicators and presented restricted cubic spline plots **(Figure 4B and Figure S10A)**. In female patients, potential mortality associations were observed for L3SFA, L3VFA, L1SFD, L1VFD, L3 subcutaneous fat index (L3SFI), and L3 visceral fat index (L3VFI) **(Figure 4C)**. Similarly, we identified optimal cutoff values for these indicators and visualized the findings through RCS plots **(Figure 4D and Figure S10B)**.

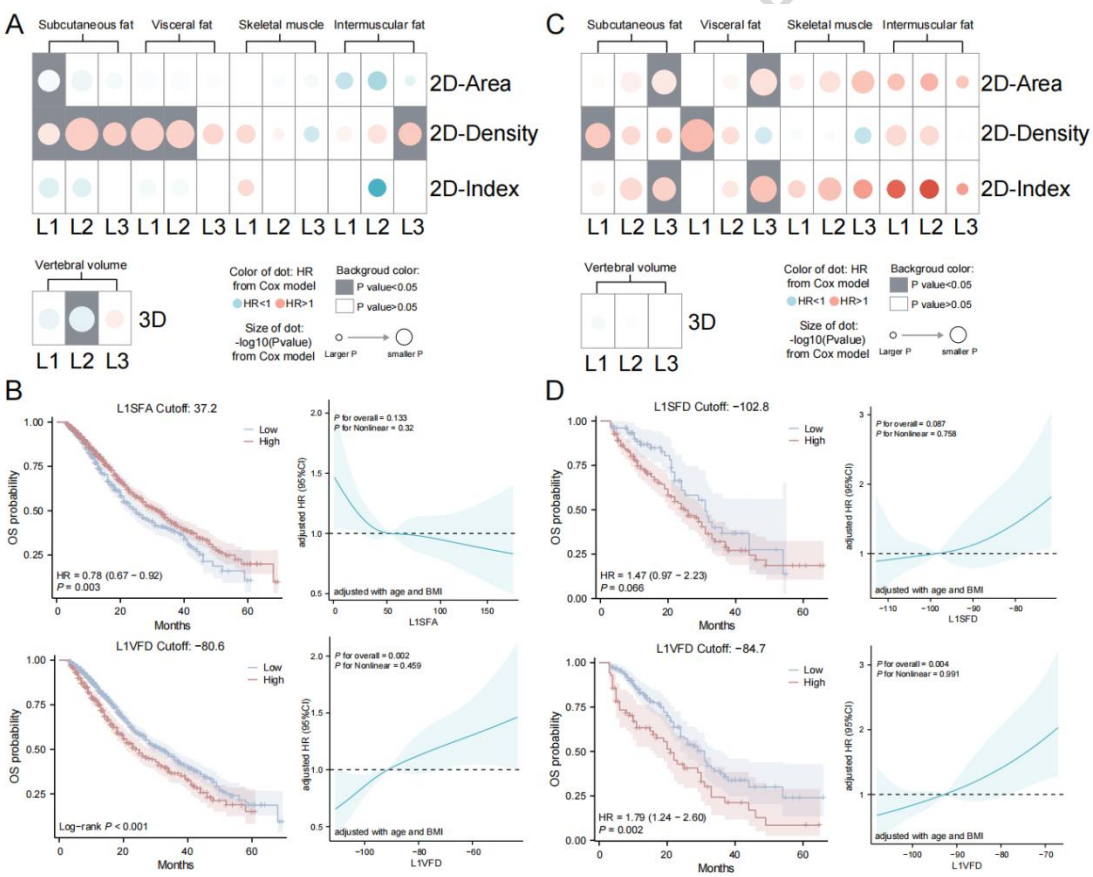

Figure 4. Association between multidimensional abdominal body composition and survival outcomes. (A) The heatmap shows the results of univariate Cox regression analysis between multidimensional abdominal body composition parameters and clinical outcomes in males. (B) Survival curves illustrate survival differences based on specific abdominal body composition parameters in male patients, and restricted cubic spline plots

depict the overall association between specific thoracic body composition parameters and survival in female patients. (C) The heatmap shows the results of univariate Cox regression analysis between multidimensional abdominal body composition parameters and clinical outcomes in females. (D) Survival curves illustrate survival differences based on specific abdominal body composition parameters in female patients, and restricted cubic spline plots depict the overall association between specific abdominal body composition parameters and survival in female patients.

Identifying specific body composition parameters as independent predictors of OS

As shown in **Table 1**, multivariate Cox regression analysis adjusted for all available clinical variables (including clinical stage, age, histopathological subtypes, BMI, total bilirubin, albumin, serum calcium, NLR, and PLR) with multiple testing correction revealed that 15 body composition parameters in male patients maintained significant associations with mortality, demonstrating inter-parameter correlations **(Figure S11)**. Given potential collinearity between BMI/age and body composition measures (despite VIF all <4 statistically), we repeated the HR adjustments after excluding BMI and age. Following the same multiple-testing correction, 24 male-specific body composition parameters showed mortality associations. Parallel analyses in female patients employing both multivariate Cox regression models with multiple testing correction identified only L1VFD as significantly associated with mortality, although 7 parameters showed prognostic relevance before correction **(Table S2)**.

Multidimensional body composition is associated with tumor molecular features

Given the close association between immunotherapy efficacy and both the extent of intratumoral immune infiltration and the expression of immune checkpoint molecules, we conducted a correlation analysis between immune checkpoint molecule expression and multidimensional body composition parameters, followed by clustering of the resulting correlation coefficients. The results showed that, in both male and female patients from the NSCLC-Radiogenomics cohort, specific correlation modules clustered together. Similar clustering patterns were also observed for immune

infiltration **(Figure 5A)**. These findings were further validated in the TCGA cohort **(Figure S12A)**. To visualize the relationships, we constructed quadrant plots based on the correlation coefficients among body composition parameters, CD274 (PD-L1) expression, and immune score (representing immune infiltration). In male patients, parameters such as IMFA and IMFV showed positive correlations with both CD274 and immune score, while SMV, SMA, and SFD exhibited negative correlations. This trend is highly consistent with the clinical outcomes previously observed in lung cancer patients receiving immunotherapy. In female patients, indicators such as IMFD were predominantly located in the second quadrant, showing a negative correlation with CD274 expression, which aligns with the findings from the clinical cohort **(Figure 5B)**. Similar trends were also observed in the TCGA cohort **(Figure S12B)**. Further investigation via GSEA revealed that in male patients, elevated T9IMFA was associated with the activation of pathways such as the "T Cell Receptor Signaling Pathway," whereas increased T8SFD was linked to the suppression of the "Interferon Alpha Beta Signaling" pathway. In female patients, elevated T8SFD and T10IMFD were associated with the inhibition of pathways such as "Interferon Gamma Response" **(Figure 5C-D)**.

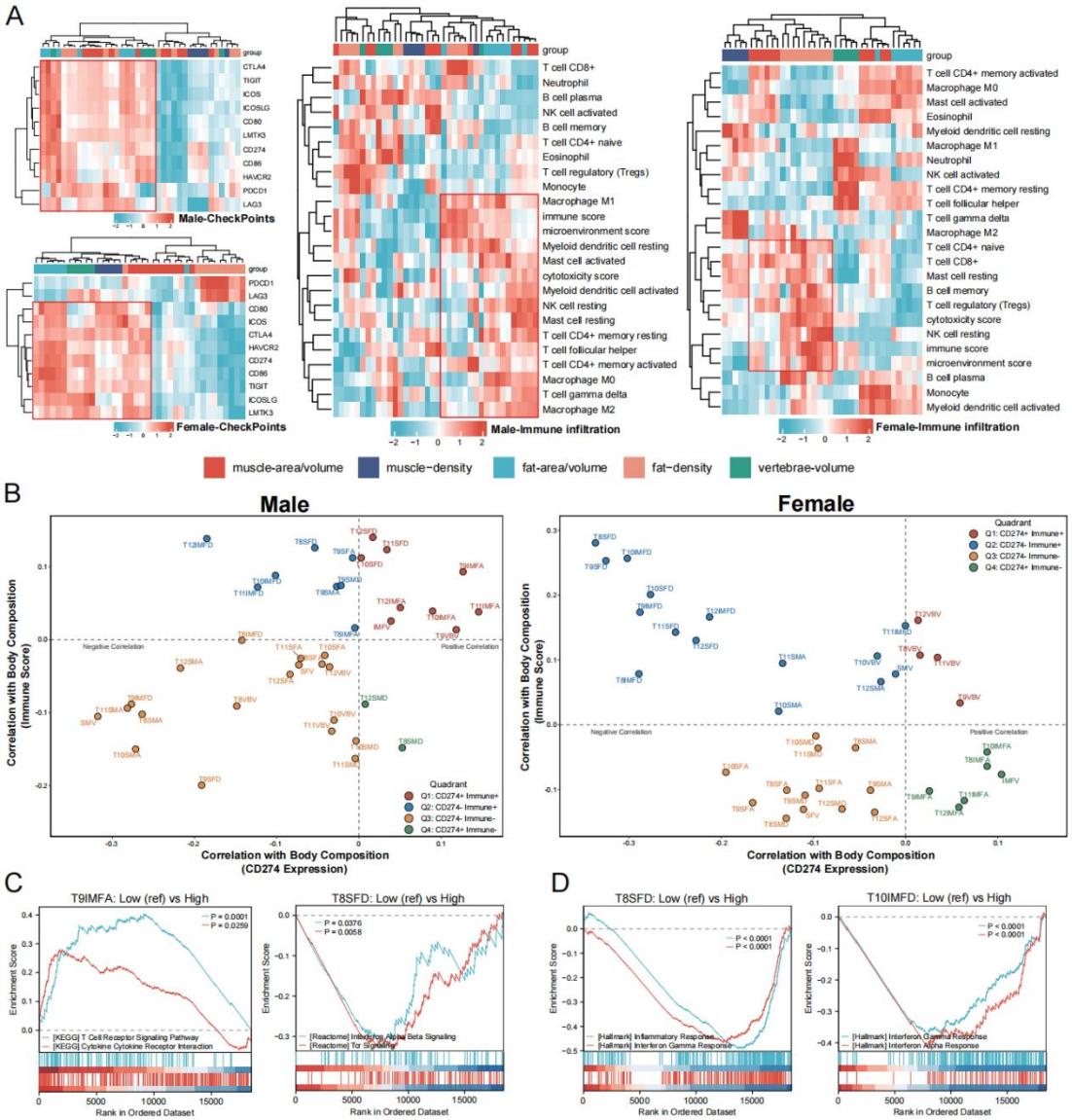

Figure 5. Multidimensional body composition is associated with tumor molecular features. (A) Heatmap showing clustering patterns of correlations between immune checkpoint expression and multidimensional body composition parameters (left panel). Heatmap showing clustering patterns of correlations between intratumoral immune infiltration and multidimensional body composition parameters (right panel). (B) Quadrant plots illustrating the correlations between multidimensional body composition parameters and CD274 expression, as well as between multidimensional body composition parameters and immune score (male: left panel; female: right panel). (C) GSEA showing the association between male-specific body composition parameters and pathway activity. (D) GSEA showing the association between female-specific body

composition parameters and pathway activity.

ScRNA-seq elucidates the association between body composition and immune microenvironment

To further explore the association between body composition and the intratumoral immune microenvironment, scRNA-seq data were analyzed **(Table S3)**. Specifically, data were obtained from 23 NSCLC samples (male n=12, female n=11). Using canonical marker genes, we annotated the cell populations as T/NK cells, epithelial cells, myeloid cells, B cells, fibroblasts, plasma cells, proliferative cells, endothelial cells, and mast cells **(Figure 6A-B)**, and their distribution was found to be similar between male and female samples **(Figure S13)**. We focused our analysis on IMFV, a representative body composition parameter in male patients. Subsequently, we performed more detailed annotation of T/NK cells, classifying them into NK cells, CD4T cells, CD8T cells, and Treg cells. The proportions of these subsets did not differ significantly between male patients with high versus low IMFV **(Figure 6C)**. Pathway analysis revealed that the "Interferon Alpha/Beta Signaling" pathway was significantly enriched in CD8T cells from the high-IMFV group, and interferon-related pathways were also up-regulated in NK cells **(Figure S14)**. The exhaustion scores of both CD8T cells and NK cells were lower in the high-IMFV male group **(Figure 6D)**. Pathway analysis using the Hallmark gene set revealed that the "Oxidative Phosphorylation" pathway was upregulated in CD8T cells from the high-IMFV male group **(Figure S15)**. Next, we performed detailed annotation of myeloid cells **(Figure 6E)**, classifying them into dendritic cells (DCs), monocytes, and macrophages. No significant differences in the proportions of these subsets were observed between the high- and low-IMFV groups. However, antigen presentation in DCs was found to be upregulated in the high-IMFV male group **(Figure 6E)**, and similarly, the "Oxidative Phosphorylation" pathway in DCs was also enhanced **(Figure S16)**. In macrophages from the high-IMFV male group, we observed higher M1 scores and lower M2 scores **(Figure 6F)**, along with upregulation of interferon-related

pathways and Oxidative Phosphorylation **(Figure S17)**. **Figure 6G** presents two representative patients illustrating distinct body composition and immune infiltration profiles. We also examined the expression of immune checkpoint molecules (LAG3, PD-1, and TIM-3), which were predominantly expressed in T/NK subpopulations. Overall, checkpoint expression was lower in the high-IMFV male group, indicating a potentially lower level of exhaustion **(Figure 6H)**.

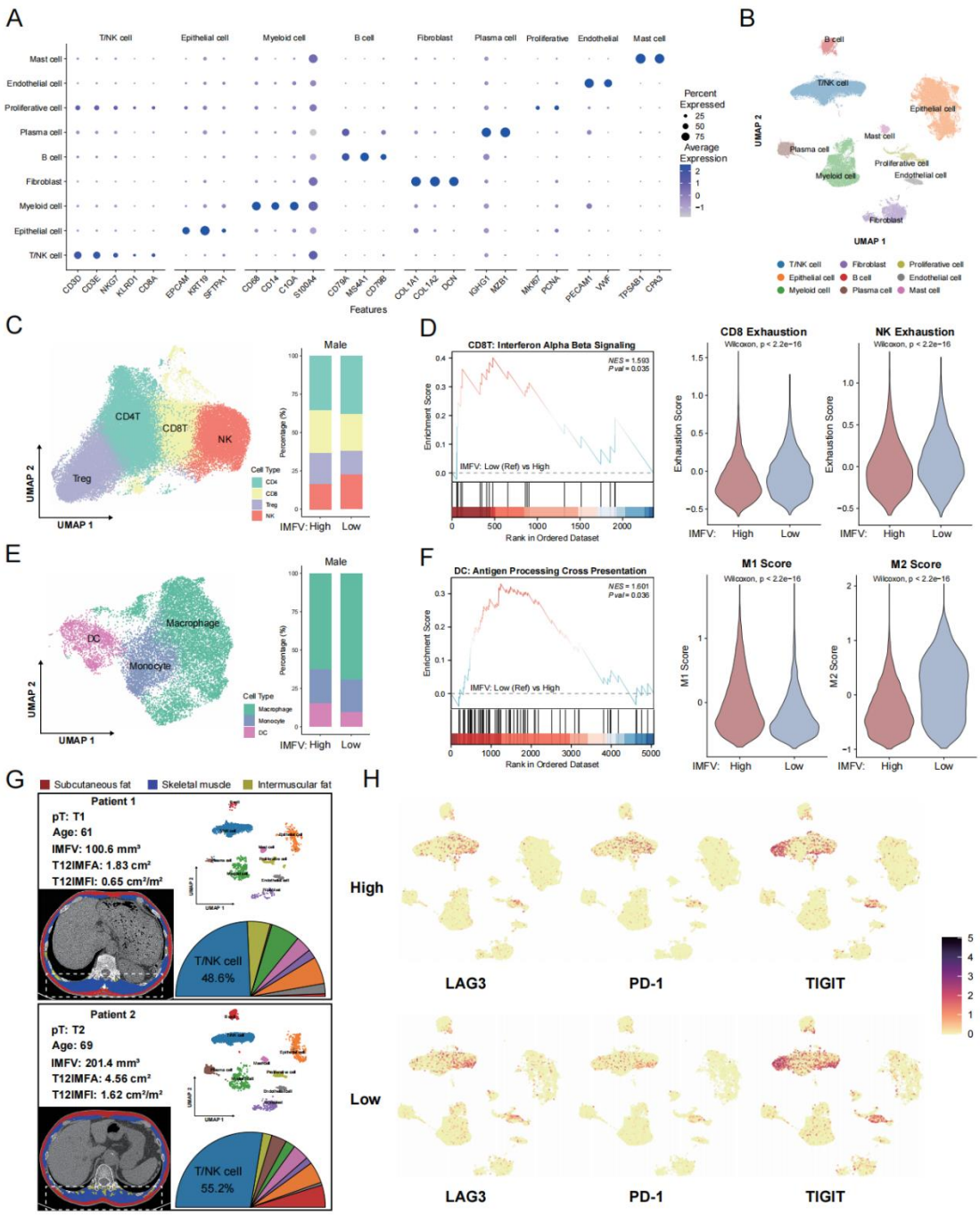

Figure 6. ScRNA-seq elucidates the association between body composition and immune microenvironment. (A) Canonical marker-based annotation was performed to identify major cellular subsets. (B) Initial clustering categorized cell populations into T/NK cells, epithelial cells, myeloid cells, B cells, fibroblasts, plasma cells, proliferative cells, endothelial cells, and mast cells. (C) Re-clustering of T/NK cells delineated NK cells, CD4+ T cells, CD8+ T cells, and regulatory T cells (Tregs) (left panel), with their proportional distribution across IMFV-high and IMFV-low

groups shown (right panel). (D) GSEA revealed enhanced interferon pathway activity in CD8T cells from IMFV-high males (left panel), while violin plots demonstrated significantly lower exhaustion scores in both CD8T cells and NK cells of IMFV-high males versus IMFV-low males (right panel). (E) Myeloid cell re-clustering identified dendritic cells, monocytes, and macrophages (left panel), with their proportional distribution across IMFV groups displayed (right panel). (F) GSEA showed upregulated antigen processing cross presentation pathways in dendritic cells from IMFV-high males (left panel), with violin plots illustrating higher M1 scores and lower M2 scores in macrophages of IMFV-high males (right panel). (G) Comparative case presentations demonstrate cellular distribution patterns between representative IMFV-high and IMFV-low male patients. (H) Differential expression patterns of immune checkpoint molecules between IMFV-high and IMFV-low male groups.

We next examined the representative body composition parameter T12SFD in female patients. In females with high T12SFD, no significant differences were observed in CD8T cell or NK cell exhaustion scores; however, higher M1 scores and lower M2 scores were detected **(Figure S18A-B)**. Furthermore, we investigated the potential biological implications of IMFV in female patients and found that high IMFV in females was associated with higher exhaustion scores in T cells and NK cells, opposite to what was observed in males. However, consistent with findings in male patients, high IMFV in females was also linked to increased M1 scores and decreased M2 scores **(Figure S18C-D)**.

Discussion

This study systematically investigated clinical outcomes in NSCLC patients treated ICIs by integrating multidimensional body composition measurements, CT image analysis, bulk RNA-seq, and scRNA-seq data. Our findings demonstrate that specific body composition parameters are not only closely associated with patient survival prognosis but also exhibit clear sex differences and location variations patterns. For example, in male patients, higher IMFV or IMFA was generally linked to better OS; while in female patients, indicators such as L3SFA and L1VFD showed potential associations with OS. These findings suggest that traditional single metrics like BMI may be

insufficient for comprehensively evaluating prognosis in NSCLC patients, and multidimensional body composition measurements can provide more accurate predictive information. Therefore, multidimensional body composition may serve as a non-invasive biomarker for pre-ICI risk stratification and holds clinical translational potential, either alone or in combination with existing indicators to build integrated predictive models.

Furthermore, our study revealed the impact of different body composition parameters on the tumor microenvironment. Specifically, male patients with high IMFV exhibited activation of the T cell receptor signaling pathway, significant upregulation of interferon-related pathways in NK cells, and lower exhaustion scores in both CD8T cells and NK cells. This suggests that specific body composition characteristics may influence treatment efficacy by modulating the effectiveness of immune responses, consistent with previous studies [12]. In female patients, although the high-IMFV group showed higher fatigue scores in CD8T cells or NK cells, they also demonstrated higher M1 macrophage scores and lower M2 scores, which aligns with better prognosis. This finding challenges previous views that fat directly promotes cancer [20]. Notably, we also detected increased oxidative phosphorylation activity in CD8T cells and DCs in high-IMFV patients. We thus speculate that the protective effect of intermuscular fat may arise from its immunometabolic regulatory function, whereby free fatty acids derived from this depot serve as energy substrates for immune cells [21], promoting anti-tumor immune responses through activation of the oxidative phosphorylation pathway, ultimately improving response to immunotherapy. This was validated at the bulk RNA-seq, showing that patients with higher T9IMFA had greater activation of the T Cell Receptor Signaling Pathway.

From the perspective of adaptive immune resistance [22], tumors with stronger immune activity may secrete more anti-tumor factors such as IFN-gamma, which induces high expression of PD-L1 in tumor tissues to promote immune escape [23]. Our observation of interferon activation in CD8T cells at the single-cell level may relate to this phenomenon and correlates with PD-L1 overexpression observed at the bulk level, ultimately resulting in an immune score-positive

and PD-L1-positive state. This condition has been shown to significantly improve responses to lung cancer immunotherapy [24]. Notably, the associations between body composition and alterations in immune cell states or specific pathway mechanisms revealed through transcriptomic data (including both bulk RNA-seq and scRNA-seq) represent exploratory hypotheses. Our analyses are correlational rather than causal, and may be limited by the small sample size of the scRNA-seq cohort; therefore, validation in larger, independent datasets is needed.

The AI-driven framework for multidimensional body composition quantification developed in this study offers a clear advantage over traditional L3-level analyses. The 92 metrics (spanning from T8 to L3 vertebral levels) not only ensure comprehensive anatomical coverage but also reveal "location variations" in body composition distribution. For instance, in univariate Cox regression analysis, only T11SFA at the thoracic level showed prognostic significance, whereas other thoracic levels did not. This finding underscores that the biological and clinical relevance of body composition is inherently location-dependent, highlighting the importance of moving beyond single-level assessment toward integrated, multidimensional profiling in clinical research and practice.

We also identified significant sex differences, for example, in univariate Cox regression analysis, while subcutaneous fat was protective in males (such as L1SFA), it was a risk factor in females (such as L3SFA). Furthermore, the survival benefit associated with intermuscular fat observed in male patients was not present in females. These differences may stem from sex-based variations in sex hormones, gene expression patterns, and immune system composition [25,26]. Estrogen and testosterone, for example, are known to modulate adipose tissue distribution and function [27,28], which may indirectly shape distinct patterns of tumor-immune interactions across sexes. These findings are consistent with previous studies, suggesting that sex differences may shape distinct immune microenvironments, thereby contributing to heterogeneity in immunotherapy outcomes [29,30].

Methodologically, this study holds strengths. The nnUNet-based automated segmentation system improved

measurement efficiency by at least 100-fold and showed high consistency with traditional manual segmentation (ICC>0.87), laying a technical foundation for large-scale clinical implementation. Moreover, by integrating eight independent cohorts comprising 2,132 patients, this study constructed the largest global dataset on body composition in NSCLC immunotherapy to date, significantly surpassing previous studies [6,31-33]. The inclusion of bulk RNA-seq and scRNA-seq cohorts provides big-data and cross-scale evidence for the study's conclusions.

This study has several limitations. A predominantly retrospective design may introduce selection bias, although we partially mitigated this through automated algorithms, multi-center data, and a prospective scRNA-seq cohort. Gender imbalance (only 15.2% female) may reduce statistical power in the female subgroup; therefore, we consider the findings in the female subgroup as preliminary and exploratory, necessitating future validation in larger female cohorts to confirm the generalizability of these body composition parameters. Additionally, the causal relationship between dynamic changes in body composition and ICI efficacy remains unclear and should be further validated through interventional clinical trials (such as exercise/nutrition programs combined with ICI therapy). In the future, we will establish a multi-center prospective cohort to regularly monitor dynamic changes in body composition, control for potential confounders (including comorbidities and prior treatment history), integrate circulating biomarker analyses, and develop an automated clinical decision-making system based on CT imaging.

In conclusion, this study highlights the importance of multidimensional body composition in the management of NSCLC patients, providing new insights for optimizing immunotherapy strategies. At the same time, it clarifies the significant "sex differences" and "location variations" between body composition and immunotherapy outcomes and reveals the mechanism by which intermuscular fat exerts a protective effect in male patients through remodeling of the tumor immune microenvironment.

Methods

Cohorts and patients

This study was conducted in accordance with the principles of the Declaration of Helsinki and adhered to the Transparent Reporting of a Multivariable Prediction Model for Individual Prognosis or Diagnosis (TRIPOD) reporting guidelines [34]. Ethical approval was granted by the Institutional Review Boards of: Union Hospital Affiliated to Tongji Medical College of Huazhong University of Science and Technology (WHUH, No. 0482), Affiliated Hospital of Nantong University (AHNMC, No. 2018-K020), the 900th Hospital of the Joint Logistics Support Force of the People's Liberation Army (900thPH, No. 2023-097), the First Affiliated Hospital of Guangzhou Medical University (GYFYY, No. ES-2024-K173-01), and the First Affiliated Hospital of Hainan Medical University (HYFY, No. 2023-275). The ethics committee of each participating center waived the requirement for informed consent. Inclusion criteria were: (1) Clinically and pathologically confirmed stage III and IV NSCLC; (2) absence of other primary malignancies; (3) receiving immune checkpoint inhibitor (s); (4) availability of baseline chest CT scans prior to the first ICI treatment. Exclusion criteria were: (1) incomplete clinical or follow-up data; (2) poor CT imaging quality or imaging unsuitable for assessment; (3) receiving other anti-tumor treatments before immunotherapy. To further examine associations between tumor biology and body composition, we incorporated two publicly available cohorts with paired CT imaging and transcriptomic data (NSCLC-Radiogenomics and TCGA-LUAD/LUSC). Furthermore, we established a prospective cohort (Radiogenomics-Lung, NCT06500312, first posted July 15, 2024; sponsor: Union Hospital, Tongji Medical College, Huazhong University of Science and Technology) containing paired CT imaging and NSCLC scRNA-seq data to comprehensively investigate relationships between intratumoral immune microenvironment and radiologically-derived body composition.

A total of 2,132 NSCLC patients across eight independent cohorts were included in this study. Detailed inclusion/exclusion criteria and patient recruitment processes for each cohort are summarized in **Figure S19**. The

primary clinical outcome was overall survival (OS), defined as the time from initiation of immunotherapy to death from any cause. Follow-up was conducted through routine clinical electronic records, with supplemental telephone follow-ups performed when electronic records provided insufficient information to determine clinical outcomes.

Multidimensional body composition measurement and evaluation

Multidimensional body composition measurements were performed for all NSCLC patients using a standardized analytical pipeline designed to quantify 92 distinct two-dimensional (2D) and three-dimensional (3D) parameters from pretreatment CT scans. First, based on a pre-trained nnUNet model [35], vertebral segmentation was performed on the images, including all detectable thoracic and lumbar vertebrae. For each individual vertebra, its spatial coordinates (X, Y, Z) and volumetric data were obtained. Second, using another pre-trained nnUNet model [35] was used to segment four key body composition compartments: subcutaneous fat, skeletal muscle, intermuscular fat, and visceral fat. To ensure comparability, all body composition measurements were standardized within a common anatomical reference range from the superior border of the T8 vertebra to the inferior border of the L3 vertebra. The volume of each body composition compartment within this T8-L3 span was calculated. The rationale for selecting the T8-L3 range rather than a single L3 slice was to comprehensively capture body composition distribution while ensuring coverage by most routine CT scans, thereby maximizing sample size and improving statistical power. Using the mid-vertebral plane Z-coordinates, single-slice body composition segmentation data were obtained to calculate cross-sectional areas, which were then normalized by height to derive corresponding body composition index. Density measurements were obtained by integrating original image data with segmentation masks. In total, 92 body composition parameters across 16 categories were acquired, with detailed calculation formulas and measurement methods provided in **Table S4**. To minimize variability, body composition above T7 was excluded from analysis, as it can be significantly influenced by arm positioning during the CT scan **(Figure S20)**. Furthermore, because not all patients in the public and prospective

sequencing cohorts had complete scans covering the L1-L3 region, the analysis for the NSCLC-Radiogenomics, TCGA, and scRNA-seq cohorts was restricted to T8-T12 body composition data. All segmentation and computational analyses were performed on a Linux system (Ubuntu 22.04) equipped with RTX 4090 GPU acceleration.

To evaluate the reliability of our body composition measurements, 50 randomly selected patients were assessed by an experienced thoracic radiologist (Q.S., 15 years' experience) who performed manual measurements of subcutaneous fat area (SFA), visceral fat area (VFA), skeletal muscle area (SMA), and intermuscular fat area (IMFA) at the L3 level. The results showed high agreement between these manual measurements and the corresponding AI-based automated measurements **(Figure S21A)**, along with significantly reduced processing time **(Figure S21B)**. Therefore, subsequent analyses exclusively used AI-derived body composition measurements, which also helped minimize potential selection bias. Furthermore, we observed similar distributions of subcutaneous fat volume (SFV), skeletal muscle volume (SMV), and intermuscular fat volume (IMFV) across five independent ICI prognostic cohorts **(Figure S22)**, supporting the robustness of our measurement protocol.

Bulk RNA-seq data analysis

The transcriptomic data were derived from the NSCLC-Radiogenomics and TCGA-LUAD/LUSC cohorts. The NSCLC-Radiogenomics cohort includes transcriptomic profiles of 130 NSCLC patients, available from GEO accession (GSE103584). Transcriptomic data for TCGA-LUAD/LUSC were downloaded from the TCGA Data Portal (https://portal.gdc.cancer.gov/), and samples with corresponding CT imaging were selected. As in previous studies [36], differential expression analysis was performed using the R package "DESeq2". Tumor-infiltrating immune cell abundances were estimated using CIBERSORT for 22 distinct immune cell types. Immune scores and microenvironment scores were further computed with the XCELL algorithm, while cytotoxicity scores were derived using MCPcounter. To investigate the relationships between multidimensional body composition and both

intratumoral immune infiltration and immune checkpoint expression, we generated four-quadrant plots based on correlation coefficients between CD274 (PD-L1) and body composition parameters, as well as between immune scores and body composition parameters. Furthermore, we performed gene set enrichment analysis (GSEA) using the KEGG, Reactome, and Hallmark databases to identify biological pathways associated with different body composition profiles.

ScRNA-seq data analysis

Through surgical resections or biopsies, 23 fresh NSCLC samples were collected and RNA sequencing libraries were constructed using a reverse transcription sequencing protocol. Single-cell sequencing was performed on the 10× Chromium or DNBelab C4 platforms. In R, following previously published guidelines (29608179), scRNA-seq data was analyzed using Seurat. Low-quality cells were filtered out if they expressed fewer than 300 genes, exhibited mitochondrial content exceeding 10%, or contained more than 1% red blood cell markers. Standard preprocessing steps included normalization (NormalizeData), identification of highly variable features (FindVariableFeatures), and data scaling (ScaleData). The Harmony method was applied for batch effect correction. Uniform Manifold Approximation and Projection (UMAP) was utilized for dimensional reduction to summarize the main principal components, with different cell types annotated using the Dimplot function. Initial clustering identified T/NK cells, Epithelial cells, Myeloid cells, B cells, Fibroblasts, Plasma cells, Proliferative cells, Endothelial cells, and Mast cells. Subsequently, T/NK cells and myeloid cells underwent secondary clustering. The ssGSEA method was employed to assess the exhaustion scores of CD8 T cells and NK cells, as well as the M1 and M2 scores of macrophages; the gene sets used can be found in **Table S5**. Based on the KEGG, Reactome, and Hallmark databases, GSEA was conducted to identify pathways involved in CD8T cells, NK cells, DC cells, and macrophages under different body composition conditions.

Statistical analysis

Statistical analyses were performed using R (version 4.2), SPSS (version 26.0), and GraphPad Prism (version 8.0). Continuous variables are presented as mean ± standard deviation (SD) or median (IQR), while categorical variables are expressed as counts and percentages. The agreement between manual and AI measurements of body composition was evaluated using intraclass correlation coefficient (ICC) and Bland-Altman plots. Group comparisons were conducted using the Wilcoxon rank-sum test or Student’s t-test for continuous variables, and the Chi-square test or Fisher’s exact test for categorical variables. The Spearman correlation test was used to examine correlations between body composition parameters and between body composition and intratumoral immune cells or immune checkpoint molecule expression. Survival differences were visualized with Kaplan-Meier curves and compared using the log-rank test. For continuous body composition variables, optimal cut-off values for survival stratification were determined with the surv_cutpoint function from the survminer package, selecting the threshold that minimized the P value. Proportional hazards assumptions were checked to ensure suitability for Cox regression. Hazard ratios (HR) for specific body composition parameters were adjusted for all clinical factors (clinical stage, age, histopathological subtypes, BMI, total bilirubin, albumin, serum calcium, NLR, and PLR) or partial clinical factors (clinical stage, histopathological subtypes, total bilirubin, albumin, serum calcium, NLR, and PLR) to determine the predictive value of body composition. For the association analyses between body composition parameters and survival outcomes, the Benjamini-Hochberg method was used to control the false discovery rate. After adjusting for age or BMI in multivariate regression models, we also plotted restricted cubic spline (RCS) graphs for specific body composition parameters to observe their association with mortality risk. A two-sided *P*-value <0.05 was considered statistically significant.

Data Availability Statement

The data that support the findings of this study are available on request from the corresponding author.

Acknowledgements

This work was supported by the Noncommunicable Chronic Diseases-National Science and Technology Major Project (2024ZD0522800/2024ZD0522806), the key project of Hubei provincial Natural Science Foundation (2023BCB014), the National Nature Science Foundation of China (No. 82172034, No. 82472058). The funders of this study had no role in study design, data collection, data analysis, data interpretation, or writing of this report.

Authors' Contributions

YG, BG and JL conceived the project. YG, BG, JL, YP, QS and SP performed investigation. LW, YC, XL, PM, QW, QS, and SP assisted in study design and data curation. YG, BG and JL performed data analysis. LW collected human samples. YG, BG and JL wrote the original draft of the manuscript. CZ and LY were responsible for project management and supervision. LW, YC, XL, PM, QW, QS, SP, CZ and LY reviewed and edited the manuscript. All authors have approved and reviewed the final manuscript.

Conflicts of Interest

The authors declare no conflict of interest.

Reference

1. Sung H, Ferlay J, Siegel RL, et al. Global Cancer Statistics 2020: GLOBOCAN Estimates of Incidence and Mortality Worldwide for 36 Cancers in 185 Countries. *CA Cancer J Clin*. 2021;71(3):209-249. doi:10.3322/caac.21660

2. Theelen WSME, Peulen HMU, Lalezari F, et al. Effect of Pembrolizumab After Stereotactic Body Radiotherapy vs Pembrolizumab Alone on Tumor Response in Patients With Advanced Non-Small Cell Lung Cancer: Results of the PEMBRO-RT Phase 2 Randomized Clinical Trial. *JAMA Oncol*. 2019;5(9):1276-1282.

doi:10.1001/jamaoncol.2019.1478

3. Guo G, Wang Y, Zhou Y, et al. Immune cell concentrations among the primary tumor microenvironment in colorectal cancer patients predicted by clinicopathologic characteristics and blood indexes. *J Immunother Cancer*. 2019;7(1):179. doi:10.1186/s40425-019-0656-3

4. Nakao S, Arai Y, Tasaki M, et al. Intratumoral expression of IL-7 and IL-12 using an oncolytic virus increases systemic sensitivity to immune checkpoint blockade. *Sci Transl Med*. 2020;12(526)doi:10.1126/scitranslmed.aax7992

5. Wattenberg MM, Beatty GL. Overcoming immunotherapeutic resistance by targeting the cancer inflammation cycle. *Semin Cancer Biol*. 2020;65:38-50. doi:10.1016/j.semcancer.2020.01.002

6. Chaunzwa TL, Qian JM, Li Q, et al. Body Composition in Advanced Non-Small Cell Lung Cancer Treated With Immunotherapy. *JAMA Oncol*. 2024;10(6):773-783. doi:10.1001/jamaoncol.2024.1120

7. Fleming CA, O'Connell EP, Kavanagh RG, et al. Body Composition, Inflammation, and 5-Year Outcomes in Colon Cancer. *JAMA Netw Open*. 2021;4(8):e2115274. doi:10.1001/jamanetworkopen.2021.15274

8. Berardi G, Antonelli G, Colasanti M, et al. Association of Sarcopenia and Body Composition With Short-term Outcomes After Liver Resection for Malignant Tumors. *JAMA Surg*. 2020;155(11):e203336. doi:10.1001/jamasurg.2020.3336

9. Bader JE, Wolf MM, Lupica-Tondo GL, et al. Obesity induces PD-1 on macrophages to suppress anti-tumour immunity. *Nature*. 2024;630(8018):968-975. doi:10.1038/s41586-024-07529-3

10. Wang Z, Aguilar EG, Luna JI, et al. Paradoxical effects of obesity on T cell function during tumor progression and PD-1 checkpoint blockade. *Nat Med*. 2019;25(1):141-151. doi:10.1038/s41591-018-0221-5

11. Gazourian L, Durgana CS, Huntley D, et al. Quantitative Pectoralis Muscle Area is Associated with the Development of Lung Cancer in a Large Lung Cancer Screening Cohort. *Lung*. 2020;198(5):847-853.

doi:10.1007/s00408-020-00388-5

12. Cury SS, de Moraes D, Oliveira JS, et al. Low muscle mass in lung cancer is associated with an inflammatory and immunosuppressive tumor microenvironment. *J Transl Med*. 2023;21(1):116. doi:10.1186/s12967-023-03901-5

13. Cortellini A, Ricciuti B, Vaz VR, et al. Prognostic effect of body mass index in patients with advanced NSCLC treated with chemoimmunotherapy combinations. *J Immunother Cancer*. 2022;10(2)doi:10.1136/jitc-2021-004374

14. Blanc-Durand P, Campedel L, Mule S, et al. Prognostic value of anthropometric measures extracted from whole-body CT using deep learning in patients with non-small-cell lung cancer. *Eur Radiol*. 2020;30(6):3528-3537. doi:10.1007/s00330-019-06630-w

15. Takenaka Y, Oya R, Takemoto N, Inohara H. Predictive impact of sarcopenia in solid cancers treated with immune checkpoint inhibitors: a meta-analysis. *J Cachexia Sarcopenia Muscle*. 2021;12(5):1122-1135. doi:10.1002/jcsm.12755

16. Stern JH, Rutkowski JM, Scherer PE. Adiponectin, Leptin, and Fatty Acids in the Maintenance of Metabolic Homeostasis through Adipose Tissue Crosstalk. *Cell Metab*. 2016;23(5):770-784. doi:10.1016/j.cmet.2016.04.011

17. Lettieri-Barbato D, Aquilano K. Aging and Immunometabolic Adaptations to Thermogenesis. *Ageing Res Rev*. 2020;63:101143. doi:10.1016/j.arr.2020.101143

18. Bekkelund SI, Jorde R. Alanine Aminotransferase and Body Composition in Obese Men and Women. *Dis Markers*. 2019;2019:1695874. doi:10.1155/2019/1695874

19. Kichenadasse G, Miners JO, Mangoni AA, Rowland A, Hopkins AM, Sorich MJ. Association Between Body Mass Index and Overall Survival With Immune Checkpoint Inhibitor Therapy for Advanced Non-Small Cell Lung Cancer. *JAMA Oncol*. 2020;6(4):512-518. doi:10.1001/jamaoncol.2019.5241

20. Park J, Euhus DM, Scherer PE. Paracrine and endocrine effects of adipose tissue on cancer development and

progression. *Endocr Rev*. 2011;32(4):550-570. doi:10.1210/er.2010-0030

21. Zhang M, Wei T, Zhang X, Guo D. Targeting lipid metabolism reprogramming of immunocytes in response to the tumor microenvironment stressor: A potential approach for tumor therapy. *Front Immunol*. 2022;13:937406. doi:10.3389/fimmu.2022.937406

22. Kim TK, Vandsemb EN, Herbst RS, Chen L. Adaptive immune resistance at the tumour site: mechanisms and therapeutic opportunities. *Nat Rev Drug Discov*. 2022;21(7):529-540. doi:10.1038/s41573-022-00493-5

23. Nirschl CJ, Suárez-Fariñas M, Izar B, et al. IFNγ-Dependent Tissue-Immune Homeostasis Is Co-opted in the Tumor Microenvironment. *Cell*. 2017;170(1)doi:10.1016/j.cell.2017.06.016

24. Sun D, Liu J, Zhou H, et al. Classification of Tumor Immune Microenvironment According to Programmed Death-Ligand 1 Expression and Immune Infiltration Predicts Response to Immunotherapy Plus Chemotherapy in Advanced Patients With NSCLC. *J Thorac Oncol*. 2023;18(7):869-881. doi:10.1016/j.jtho.2023.03.012

25. Huang Z, Chen B, Liu X, et al. Effects of sex and aging on the immune cell landscape as assessed by single-cell transcriptomic analysis. *Proc Natl Acad Sci U S A*. 2021;118(33)doi:10.1073/pnas.2023216118

26. Oliva M, Muñoz-Aguirre M, Kim-Hellmuth S, et al. The impact of sex on gene expression across human tissues. *Science*. 2020;369(6509)doi:10.1126/science.aba3066

27. Björntorp P. The regulation of adipose tissue distribution in humans. *Int J Obes Relat Metab Disord*. 1996;20(4):291-302.

28. Fanciulli G, Delitala A, Delitala G. Growth hormone, menopause and ageing: no definite evidence for 'rejuvenation' with growth hormone. *Hum Reprod Update*. 2009;15(3):341-358. doi:10.1093/humupd/dmp005

29. Sharma S, Gibbons A, Saphire EO. Sex differences in tissue-specific immunity and immunology. *Science*. 2025;389(6760):599-603. doi:10.1126/science.adx4381

30. Xiao T, Lee J, Gauntner TD, Velegraki M, Lathia JD, Li Z. Hallmarks of sex bias in immuno-oncology: mechanisms and therapeutic implications. *Nat Rev Cancer*. 2024;24(5):338-355. doi:10.1038/s41568-024-00680-z

31. Young AC, Quach HT, Song H, et al. Impact of body composition on outcomes from anti-PD1 +/- anti-CTLA-4 treatment in melanoma. *J Immunother Cancer*. 2020;8(2)doi:10.1136/jitc-2020-000821

32. Gómez-Banoy N, Ortiz EJ, Jiang CS, et al. Body mass index and adiposity influence responses to immune checkpoint inhibition in endometrial cancer. *J Clin Invest*. 2024;134(17)doi:10.1172/JCI180516

33. Yu J, Ahn H, Han KY, et al. Paradoxical Effect of Myosteatosis on the Immune Checkpoint Inhibitor Response in Metastatic Renal Cell Carcinoma. *J Cachexia Sarcopenia Muscle*. 2025;16(2):e13758. doi:10.1002/jcsm.13758

34. Collins GS, Reitsma JB, Altman DG, Moons KGM. Transparent Reporting of a multivariable prediction model for Individual Prognosis or Diagnosis (TRIPOD): the TRIPOD statement. *Ann Intern Med*. 2015;162(1):55-63. doi:10.7326/M14-0697

35. Wasserthal J, Breit H-C, Meyer MT, et al. TotalSegmentator: Robust Segmentation of 104 Anatomic Structures in CT Images. *Radiol Artif Intell*. 2023;5(5):e230024. doi:10.1148/ryai.230024

36. Gong B, Guo Y, Wan Q, et al. A Combined Model Based on Bone Mineral Density for Noninvasive Prediction of Prognosis in Non-Small Cell Lung Cancer Patients Receiving Immune Checkpoint Inhibitors: A Multicenter Retrospective Study. *MedComm (2020)*. 2025;6(10):e70398. doi:10.1002/mco2.70398

Figure Legends

Figure 1. Workflow and key findings of this study.

Figure 2. Correlations of body composition parameters in NSCLC patients. (A) Distribution patterns of subcutaneous fat volume (SFV), skeletal muscle volume (SMV), and intermuscular fat volume (IMFV) stratified by gender. (B) Correlation analyses between SFV/SMV/IMFV and age. (C)CT scanning ranges and corresponding

sample sizes. (D) Correlation analysis of different body composition parameters at the same anatomical level (upper panel), and correlation analysis of the same body composition parameter across different levels (lower panel).

Figure 3. Association between multidimensional thoracic body composition and survival outcomes. (A) The heatmap shows the results of univariate Cox regression analysis between multidimensional thoracic body composition parameters and clinical outcomes in males. (B) Survival curves illustrate survival differences based on specific thoracic body composition parameters in male patients, and restricted cubic spline plots depict the overall association between specific thoracic body composition parameters and survival in male patients. (C) The heatmap shows the results of univariate Cox regression analysis between multidimensional thoracic body composition parameters and clinical outcomes in females. (D) Survival curves illustrate survival differences based on specific thoracic body composition parameters in female patients, and restricted cubic spline plots depict the overall association between specific thoracic body composition parameters and survival in female patients.

Figure 4. Association between multidimensional abdominal body composition and survival outcomes. (A) The heatmap shows the results of univariate Cox regression analysis between multidimensional abdominal body composition parameters and clinical outcomes in males. (B) Survival curves illustrate survival differences based on specific abdominal body composition parameters in male patients, and restricted cubic spline plots depict the overall association between specific thoracic body composition parameters and survival in female patients. (C) The heatmap shows the results of univariate Cox regression analysis between multidimensional abdominal body composition parameters and clinical outcomes in females. (D) Survival curves illustrate survival differences based on specific abdominal body composition parameters in female patients, and restricted cubic spline plots depict the overall association between specific abdominal body composition parameters and survival in female patients.

Figure 5. Multidimensional body composition is associated with tumor molecular features. (A) Heatmap showing

clustering patterns of correlations between immune checkpoint expression and multidimensional body composition parameters (left panel). Heatmap showing clustering patterns of correlations between intratumoral immune infiltration and multidimensional body composition parameters (right panel). (B) Quadrant plots illustrating the correlations between multidimensional body composition parameters and CD274 expression, as well as between multidimensional body composition parameters and immune score (male: left panel; female: right panel). (C) GSEA showing the association between male-specific body composition parameters and pathway activity. (D) GSEA showing the association between female-specific body composition parameters and pathway activity.

Figure 6. ScRNA-seq elucidates the association between body composition and immune microenvironment. (A) Canonical marker-based annotation was performed to identify major cellular subsets. (B) Initial clustering categorized cell populations into T/NK cells, epithelial cells, myeloid cells, B cells, fibroblasts, plasma cells, proliferative cells, endothelial cells, and mast cells. (C) Re-clustering of T/NK cells delineated NK cells, CD4+ T cells, CD8+ T cells, and regulatory T cells (Tregs) (left panel), with their proportional distribution across IMFV-high and IMFV-low groups shown (right panel). (D) GSEA revealed enhanced interferon pathway activity in CD8T cells from IMFV-high males (left panel), while violin plots demonstrated significantly lower exhaustion scores in both CD8T cells and NK cells of IMFV-high males versus IMFV-low males (right panel). (E) Myeloid cell re-clustering identified dendritic cells, monocytes, and macrophages (left panel), with their proportional distribution across IMFV groups displayed (right panel). (F) GSEA showed upregulated antigen processing cross presentation pathways in dendritic cells from IMFV-high males (left panel), with violin plots illustrating higher M1 scores and lower M2 scores in macrophages of IMFV-high males (right panel). (G) Comparative case presentations demonstrate cellular distribution patterns between representative IMFV-high and IMFV-low male patients. (H) Differential expression patterns of immune checkpoint molecules between IMFV-high and IMFV-low male groups.

Table 1 Multivariate analyses were performed to identify the independent factors relevant to OS (Male)

Parameters	Attributes	ad HR[#] (95%CI)	*P* value[#]	ad *P* value[#]	ad HR (95%CI)[##]	*P* value[##]	ad *P* value[##]
IMFV	3D	**0.307 (0.116 - 0.811)**	**0.017***	**0.047***	**0.317 (0.135 - 0.745)**	**0.008****	**0.021***
T8IMFA	2D-Area	0.996 (0.986 - 1.006)	0.431	0.445	0.996 (0.987 - 1.004)	0.295	0.295
T8SFD	2D-Density	1.002 (0.997 - 1.008)	0.346	0.378	**1.005 (1.001 - 1.010)**	**0.029***	**0.039***
T8VBV	3D	**0.974 (0.959 - 0.990)**	**0.001*****	**0.016***	**0.973 (0.959 - 0.989)**	**< 0.001*****	**0.016***
T9IMFA	2D-Area	**0.987 (0.977 - 0.998)**	**0.018***	**0.047***	**0.989 (0.981 - 0.999)**	**0.023***	**0.035***
T9IMFI	2D-Index	0.968 (0.939 - 0.998)	0.039*	0.071	0.975 (0.950 - 1.000)	0.052	0.064
T9SFD	2D-Density	1.003 (0.998 - 1.008)	0.266	0.322	**1.005 (1.001 - 1.010)**	**0.020***	**0.034***
T9VBV	3D	**0.976 (0.962 - 0.991)**	**0.001*****	**0.016***	**0.977 (0.963 - 0.991)**	**0.002****	**0.016***
T10IMFA	2D-Area	**0.985 (0.974 - 0.996)**	**0.010****	**0.044***	**0.986 (0.976 - 0.997)**	**0.009****	**0.021***
T10IMFI	2D-Index	**0.961 (0.930 - 0.994)**	**0.021***	**0.047***	**0.965 (0.937 - 0.994)**	**0.020***	**0.034***
T10SFD	2D-Density	1.003 (0.998 - 1.007)	0.309	0.355	**1.005 (1.001 - 1.010)**	**0.024***	**0.035***
T10VBV	3D	**0.985 (0.972 - 0.998)**	**0.020***	**0.047***	**0.984 (0.971 - 0.997)**	**0.013***	**0.027***
T11IMFA	2D-Area	**0.972 (0.955 - 0.989)**	**0.002****	**0.016***	**0.972 (0.949 - 0.994)**	**0.015***	**0.029***
T11IMFI	2D-Index	**0.928 (0.882 - 0.976)**	**0.004****	**0.025***	**0.926 (0.867 - 0.989)**	**0.022***	**0.035***
T11SFA	2D-Area	0.998 (0.995 - 1.002)	0.354	0.378	0.998 (0.996 - 1.001)	0.223	0.230
T11SFD	2D-Density	1.004 (0.999 - 1.009)	0.141	0.190	**1.006 (1.002 - 1.011)**	**0.005****	**0.021***
T11SMD	2D-Density	**1.016 (1.006 - 1.026)**	**0.002****	**0.016***	**1.013 (1.003 - 1.022)**	**0.007****	**0.021***
T11VBV	3D	0.986 (0.975 - 0.998)	0.026*	0.050	**0.985 (0.973 - 0.997)**	**0.012***	**0.027***
T12IMFA	2D-Area	**0.966 (0.941 - 0.992)**	**0.009****	**0.044***	**0.975 (0.960 - 0.991)**	**0.003****	**0.019***
T12IMFI	2D-Index	**0.912 (0.847 - 0.982)**	**0.015***	**0.047***	**0.937 (0.895 - 0.981)**	**0.006****	**0.021***
T12SFD	2D-Density	1.004 (0.999 - 1.008)	0.132	0.186	**1.006 (1.002 - 1.010)**	**0.006****	**0.021***
T12SMD	2D-Density	**1.013 (1.002 - 1.023)**	**0.015***	**0.047***	**1.010 (1.001 - 1.020)**	**0.031***	**0.040***
T12VBV	3D	0.993 (0.985 - 1.000)	0.063	0.103	**0.992 (0.984 - 0.999)**	**0.029***	**0.039***
L1SFA	2D-Area	0.998 (0.995 - 1.001)	0.270	0.322	0.998 (0.996 - 1.001)	0.181	0.193
L1SFD	2D-Density	1.000 (0.995 - 1.005)	0.922	0.922	1.003 (0.999 - 1.008)	0.156	0.173
L1VFD	2D-Density	1.005 (0.999 - 1.011)	0.083	0.129	**1.008 (1.003 - 1.013)**	**0.002****	**0.016***
L2SFD	2D-Density	**1.007 (1.001 - 1.012)**	**0.023***	**0.048***	**1.008 (1.003 - 1.013)**	**0.002****	**0.016***
L2VBV	3D	**0.995 (0.991 - 0.999)**	**0.021***	**0.047***	**0.995 (0.991 - 0.998)**	**0.007****	**0.021***
L2VFD	2D-Density	1.006 (0.999 - 1.012)	0.095	0.140	**1.008 (1.002 - 1.014)**	**0.008****	**0.021***
L3IMFD	2D-Density	1.008 (0.996 - 1.019)	0.182	0.235	1.010 (0.999 - 1.021)	0.070	0.080
L3SFD	2D-Density	1.010 (0.999 - 1.020)	0.063	0.103	1.009 (1.000 - 1.018)	0.063	0.075

Note. HR[#] was adjusted with clinical stage, age, histopathological subtypes, BMI, total bilirubin, albumin, serum calcium, NLR, and PLR; HR[##] was adjusted with clinical stage, histopathological subtypes, total bilirubin; ad P value: multi-testing *P* values were adjusted by the BH method.